ELSEVIER

Contents lists available at ScienceDirect

Additive Manufacturing

journal homepage: www.elsevier.com/locate/addma





Deformation behavior of cell walls in an additively manufactured hybrid metallic foam

Xin Wang ^{a,*}, Baolong Zheng ^a, Hangman Chen ^b, Dongxu Liu ^c, Kehang Yu ^a, Benjamin E. MacDonald ^a, Lorenzo Valdevit ^a, Lizhi Sun ^c, Penghui Cao ^b, Enrique J. Lavernia ^a, Julie M. Schoenung ^a

- a Department of Materials Science and Engineering, University of California at Irvine, Irvine, CA 92697, USA
- b Department of Mechanical and Aerospace Engineering, University of California at Irvine, Irvine, CA 92697, USA
- ^c Department of Civil and Environmental Engineering, University of California at Irvine, Irvine, CA 92697, USA

ARTICLE INFO

Keywords: In-situ micromechanical testing Directed energy deposition Metallic foam Aluminum alloy Deformation behavior

ABSTRACT

A hybrid Al-Al₃Ni metallic foam was synthesized in-situ via directed energy deposition (DED) of Ni-coated Al 6061 powder, without the need for a foaming agent. Three-dimensional characterization via X-ray computed tomography shows that the foam contains approximately 61.5% porosity and a high volume fraction of the Al_3Ni phase (~60 vol. %) within the cell walls. This microstructure is notably distinct from the eutectic structure that is typically observed in conventionally processed Al-Ni alloys. To investigate the mechanical properties and deformation mechanisms of the Al-Al₃Ni cell walls, in-situ micro-pillar compression was performed, and the results reveal a notable yield strength of 560 MPa and a compressive strain that exceeds 30 %. These properties are attributable to the presence of a high volume fraction of Al₃Ni particles, in combination with the characteristics of the Al/Al₃Ni interfaces. To provide insight into the deformation mechanisms in the cell walls we used in-situ mechanical testing, transmission electron microscopy and precession electron diffraction characterization, together with molecular dynamics simulations. Our results reveal two distinct mechanisms: uniform dislocationbased deformation of the Al alloy phase and localized deformation within the slip bands in the Al_3Ni phase. The results further highlight the importance of the Al/Al₃Ni interfaces in mechanical strengthening and the transfer of plastic deformation from the Al phase to the Al₃Ni phase. At high mechanical loads, cracks form due to the large stress concentration at the slip bands and slip band intersections in the Al₃Ni, giving rise to intragranular fracture of Al₃Ni and finally interfacial debonding and cracking.

1. Introduction

As a class of functionally integrated materials (FIMs), metallic foams have engendered scientific and technical interest because of their unique combinations of high specific stiffness and strength and high plastic deformability, resulting in excellent energy absorption [1–4]. Al-based foams have attracted particular interests as functional and structural materials due to their low densities, flame resistance and acoustic insulation [5,6]. Metallic foams are typically fabricated using conventional melting and molding processes [1,2], including casting and powder metallurgy (PM) techniques, and generally require the addition of foaming agents to promote pore formation. The mechanical performance of Al-based metallic foams under compressive loads under different strain rates [7,8] and deformation temperatures [6,9,10] have

been extensively investigated. Despite their unique properties, foamed Al alloys lack sufficient strength for many applications and hence various strengthening and toughening approaches have been explored including grain boundary engineering, solid solution addition, precipitation, and particulate reinforcement strategies [1,11]. Notably, various composite metallic foams [12,13] and metal matrix syntactic foams [14–17] have been developed for higher strength and energy absorption capabilities.

In our previous study, we used directed energy deposition (DED), an additive manufacturing (AM) technique [18], to demonstrate that it is possible to use in-situ reactions to generate a porous material via AM, without the need of any foaming agents. The feedstock material used was a Ni-coated Al 6061 powder, and the result was a novel hybrid, Al-Al₃Ni metallic foam material. During DED processing, the Ni coating

E-mail address: xinw15@uci.edu (X. Wang).

^{*} Corresponding author.

reacted with the Al alloy, leading to the in-situ formation of the intermetallic compound, Al $_3$ Ni, while simultaneously forming a high volume of pores (more than 60 vol. %). These DED-deposited hybrid Al-Al $_3$ Ni metallic foams exhibited a yield strength of 190 MPa [18], which is higher than that of monolithic Al 6061 (55 MPa for annealed and 145 MPa for T4 tempered [19]), and with a significantly lower density of 1.64 g/cm 3 [18]. The cell walls of this Al-Al $_3$ Ni material exhibited a unique microstructure, distinct from that found in conventional Al-Al $_3$ Ni, containing a high volume fraction of the Al $_3$ Ni intermetallic phase uniformly dispersed in the Al 6061 phase, which was hypothesized to significantly contribute to the mechanical response as a reinforcement phase. This microstructure has heretofore never been documented in a porous matrix.

In related studies, Al-Al₃Ni composites have been reported to be more suitable for high-temperature applications than other widely used Al alloys, such as Al-Si alloys, due to their relatively high eutectic temperature of 913 K [20–22]. These composites typically exhibit a fine fiber-like Al₃Ni eutectic structure, which provides them with considerable high-temperature mechanical stability up to 773 K, a high Young's modulus, attractive chemical stability and a low coefficient of thermal expansion [22]. Al-Al₃Ni composites have also attracted attention for use in functionally graded materials (FGM) [23,24].

The objective of the present study is to address fundamental questions related to the mechanical behavior of the Al-Al₃Ni cell wall regions in the DED-deposited hybrid Al-Al₃Ni metallic foam reported in our earlier study, as the microstructure is quite distinct from the eutectic structure of conventional Al-Al₃Ni composite materials [18]. These questions include: what are the fraction and 3D spatial distribution of the pores and phases in DED-deposited hybrid Al-Al₃Ni metallic foams? How does the cell wall region in these Al-Al₃Ni metallic foams deform and contribute to the overall strength of the foam? To answer these questions, we combined advanced characterization methods with molecular dynamics (MD) simulations. Specifically, we used X-ray computed tomography (CT) for structure characterization and studied the mechanical behavior and underlying deformation mechanisms for the cell walls using micro-scale scanning electron microscopy (SEM) in-situ compressive testing. The post-mortem deformation microstructure was characterized by SEM, (scanning) transmission electron microscopy (S/TEM) and precession electron diffraction (PED). Deformation behavior of the Al-Al₃Ni system was further investigated by molecular dynamics (MD) simulation. Our analyses of the microstructure and mechanical behavior of the cell walls of the DED-deposited hybrid Al-Al₃Ni metallic foams provide fundamental insight into the design and synthesis of high-performance Al-based materials. While the energy absorption characteristics of this novel microstructure fall outside the scope of the present study, these should be characterized in future work.

2. Experimental

2.1. Sample preparation by additive manufacturing

For the fabrication of hybrid Al-Al $_3$ Ni metallic foams, a laser engineered net shaping (LENS®) Workstation 750 was used with Ni-coated Al 6061 powder (Ni content \sim 15–20 wt. %). Cubical block samples of 10 mm \times 10 mm \times 20 mm were fabricated. The hatch spacing between successive lines in a plane was 0.38 mm, the hatch pattern rotation angle was 90°, the increment in height from one layer to another was 0.25 mm, the laser output power was 250 W, the traverse speed was 17 mm/s, and the powder feed rate was 10 rpm (approximately 4 g/min).

2.2. 3D X-ray computed tomography

The size and 3D distribution of the pores in the as-deposited foams was assessed using 3D X-ray CT scans with an Xradia VersaXRM $^{\rm IM}$ 410, which can provide sub-micron resolution (900 nm). The regions of

interest in the as-deposited samples were machined out and polished with cuboid sample dimensions of 1 mm \times 1 mm \times 5 mm. The scans were carried out with 2000 projections in one full rotation, and the image reconstruction was conducted with system-supplied software.

2.3. In-situ micro-pillar compression tests

Micro-pillars \sim 7.5 μm (diameter) \times 15 μm (height) in size were fabricated from the cell wall regions of the as-deposited Al-Al₃Ni metallic foam by focused ion beam (FIB) using a dual-beam scanning electron microscope (SEM, FEI Quanta 3D, Thermo Fisher Scientific Inc., MA, USA). The length-to-diameter ratio was maintained at a value of 2:1 following the guidelines from previous studies [25,26] to avoid buckling due to higher aspect ratios and non-uniform stresses due to lower aspect ratios. To minimize the contamination from Ga and tapering effect [25, 26], the ion beam current was gradually decreased with a final FIB cleaning procedure at 10 pA. The micro-pillar design used in our study maintains a small taper angle of $\sim 2^{\circ}$. In-situ compression was performed using a Hysitron PI85 Picoindenter (Bruker Inc., Massachusetts, USA) equipped with a 20 µm diameter flat-top conical tip inside the SEM. In-situ compression was performed under displacement control mode with a displacement rate of 15 nm/s, corresponding to an initial strain rate of 1×10^{-3} s⁻¹. We tested two micro-pillars; one was compression tested to a maximum compressive displacement of 4.5 µm (i.e., 30 % engineering strain), and one was compression tested to a compressive displacement of approximately 2.65 µm (i.e., ~17.5 % engineering strain) and used for post-mortem microstructural analysis. The latter micro-pillar was lifted out and thinned by FIB for post-mortem microstructural investigation of the microstructure in the plastically deformed region. Pores were not noticed on the surface or in the interior of the micro-pillars studied during FIB milling. Post-mortem microstructural analysis was performed on a (scanning) transmission electron microscope (S/TEM, JEOL JEM-2800, JEOL USA Inc., MA, USA) operated at 200 kV. A NanoMEGAS ASTAR® precession electron diffraction (PED) system equipped on the TEM was used for orientation and local strain mapping.

2.4. Molecular dynamics simulation

An Al-Al₃Ni bi-crystal model was built to provide insight into behavior of dislocations during uniaxial compressive deformation. The top layer of the bi-crystal model is an FCC structured Al phase with an initial orientation of [100], [010] and [001] along the x, y and z directions, respectively. The bottom layer is an orthorhombic structured Al₃Ni phase with [100], [010] and [001] orientations along the x, y and z directions, respectively. To minimize the residual stresses resulting from the lattice misfit in the interface between Al and Al₃Ni, the dimensions of the Al and Al₃Ni along the interface were chosen as $38a_{Al} \times 39a_{Al}$ (i.e., $32a_{Al3Ni} \times 24b_{Al3Ni}$), where $a_{Al} = 4.046$ Å is the Al lattice constant, and $a_{Al3Ni} = 4.807$ Å and b_{Al3Ni} 6.557 Å are lattice parameters of Al₃Ni.

An embedded atom method (EAM) potential developed by Mishin was employed for the Al-Ni system [27], and the adopted a force field designed for L12 AlNi $_3$ was adopted to model the order Al $_3$ Ni. Periodic boundary conditions were applied along the three dimensions of the bi-crystal model. The model was thermally equilibrated at 300 K by an anisotropic zero-pressure isobaric-isothermal NPT ensemble for 20 ps with a MD time step of 0.002 ps. After relaxation, the bi-crystal model was compressed along the [001] direction with a constant strain rate of 5 \times 10 8 s $^{-1}$. The Large-scale Atomic/Molecular Massively Parallel Simulator (LAMMPS) was utilized to carry out molecular dynamics (MD) simulation [28], and atomic structures were visualized by the molecular visualization package OVITO [29]. The evolution of dislocations was illustrated using the Dislocation Extraction Algorithm (DXA). Because DXA is unable to identify the dislocations in the orthorhombic structure, an atomic strain modifier was used to show the evolution of the

dislocation slip-indued deformation bands in the bi-crystal system.

3. Results and discussion

3.1. Microstructure of as-deposited Al alloy foam

Our previous study demonstrated that DED deposition using Nicoated Al 6061 powder feedstock formed an Al-Al₃Ni closed cell foam structure [18]. A high volume fraction of pores develop in-situ during deposition due to the relatively low vaporization temperature of Al 6061 as compared to that of Ni. The size of the pores varies with both the processing parameters and the location within the deposits [18]. A cubical block foam sample deposited on an Al 6061 substrate is shown in Fig. 1(a). To identify the distribution and structure of pores and phases in three dimensions, the as-deposited hybrid Al-Al₃Ni metallic foam was examined using X-ray CT. A reconstructed 3D geometry of the pores is shown in Fig. 1(b). Most of the pores are spherical, with size ranging from 25 μ m to 350 μ m. Fig. 1(c) shows the 3D structure of the cell wall regions of the as-deposited hybrid Al-Al₃Ni metallic foam, with the Al phase in red and Al₃Ni phase in blue. The volume fraction of pores in the Al-Al₃Ni metallic foam approaches 61.5 vol. %.

A representative SEM secondary electron micrograph of the cell wall region is shown in Fig. 1(d). As detailed in our previous work [18], the Al $_3$ Ni phase shows a dendritic microstructure with features in the size range of 1–5 μm and an average inter-dendritic spacing of about 2 μm . The area fraction of the Al $_3$ Ni phase, which has a brighter contrast in the SEM micrograph, is $\sim\!60$ %, as quantified by the ImageJ software from the SEM micrographs. The very high fraction of Al $_3$ Ni phase embedded in the Al alloy phase is hypothesized to significantly enhance the yield strength and elastic modulus of the hybrid material. A representative TEM micrograph of the as-deposited hybrid Al-Al $_3$ Ni metallic foam is

shown in Fig. 1(e). A uniform distribution of dislocations is present in the Al alloy phase, with a dislocation density of $\sim 3.2 \times 10^{14} \, m^{-2}$, while the Al $_3$ Ni phase appears free of defects, i.e., dislocations. Fig. 1(f) is a typical high-resolution TEM image of an Al/Al $_3$ Ni interface showing the interface formed during the DED process is clean.

3.2. In-situ micro-pillar compression tests

The deformation behavior of closed cell metallic foam materials is influenced by multiple factors, including the relative density, material composition, and morphology and size of the pores [30]. The mechanical properties of bulk as-deposited hybrid Al-Al₃Ni metallic foam were systematically investigated in our previous study [18]. In the present study, we leverage in-situ micromechanical testing as an approach to probe the deformation behavior of the cell wall regions of the hybrid Al-Al₃Ni metallic foam, with a focus on the nanoscale phenomena critical for our understanding of strengthening and toughening mechanisms.

Fig. 2(a) shows the representative SEM secondary electron micrograph of the Al-Al₃Ni micro-pillars with 52° tilt relative to the electron beam. The micro-pillars were fabricated from the cell wall regions of the as-deposited hybrid Al-Al₃Ni metallic foam. The micro-pillars are $\sim\!7.5~\mu m$ in diameter and $\sim\!15~\mu m$ in height and contain multiple Al₃Ni grains embedded in the Al alloy phase. The Al₃Ni content is consistent among the micro-pillars, estimated from several SEM images of the micro-pillar surfaces, such as the one shown in Fig. 2(a), to be 61.6 \pm 1.5 %.

The micro-pillar was quasi-statically compressed inside the SEM, which allows us to observe microstructural evolution of the cell wall region during deformation while simultaneously quantifying the mechanical behavior. The engineering stress-strain curve acquired is shown

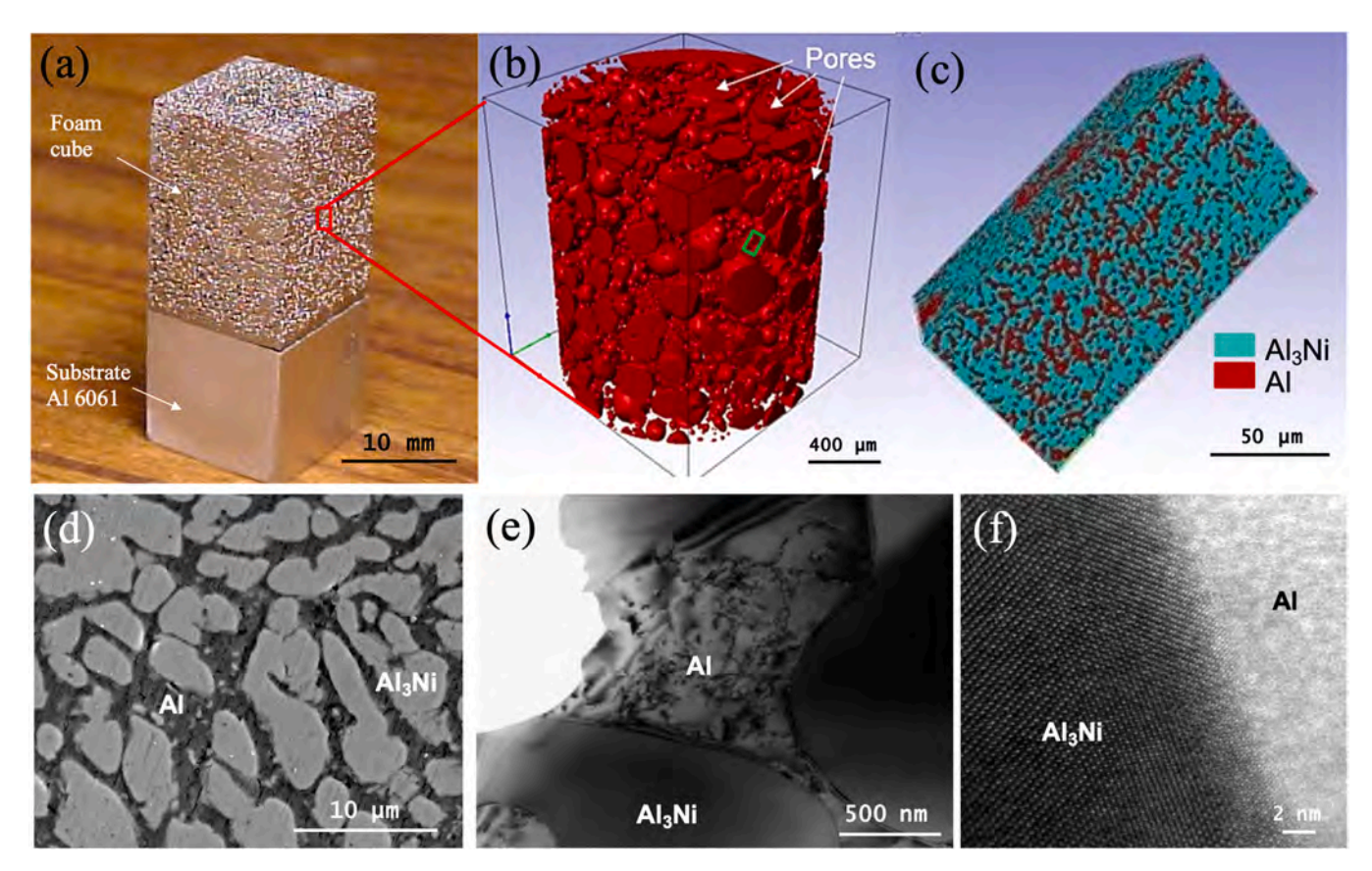


Fig. 1. Microstructure of the DED-deposited hybrid Al-Al₃Ni metallic foam: (a) Photo of the hybrid Al-Al₃Ni foam block built on an Al 6061 substrate [6]. Nano CT 3D reconstruction of (b) pores and (c) the Al and Al₃Ni phases in the cell walls. (d, e) Representative SEM secondary electron micrograph and TEM bright field image of the cell wall region. (f) High-resolution TEM image of an Al/Al₃Ni interface.

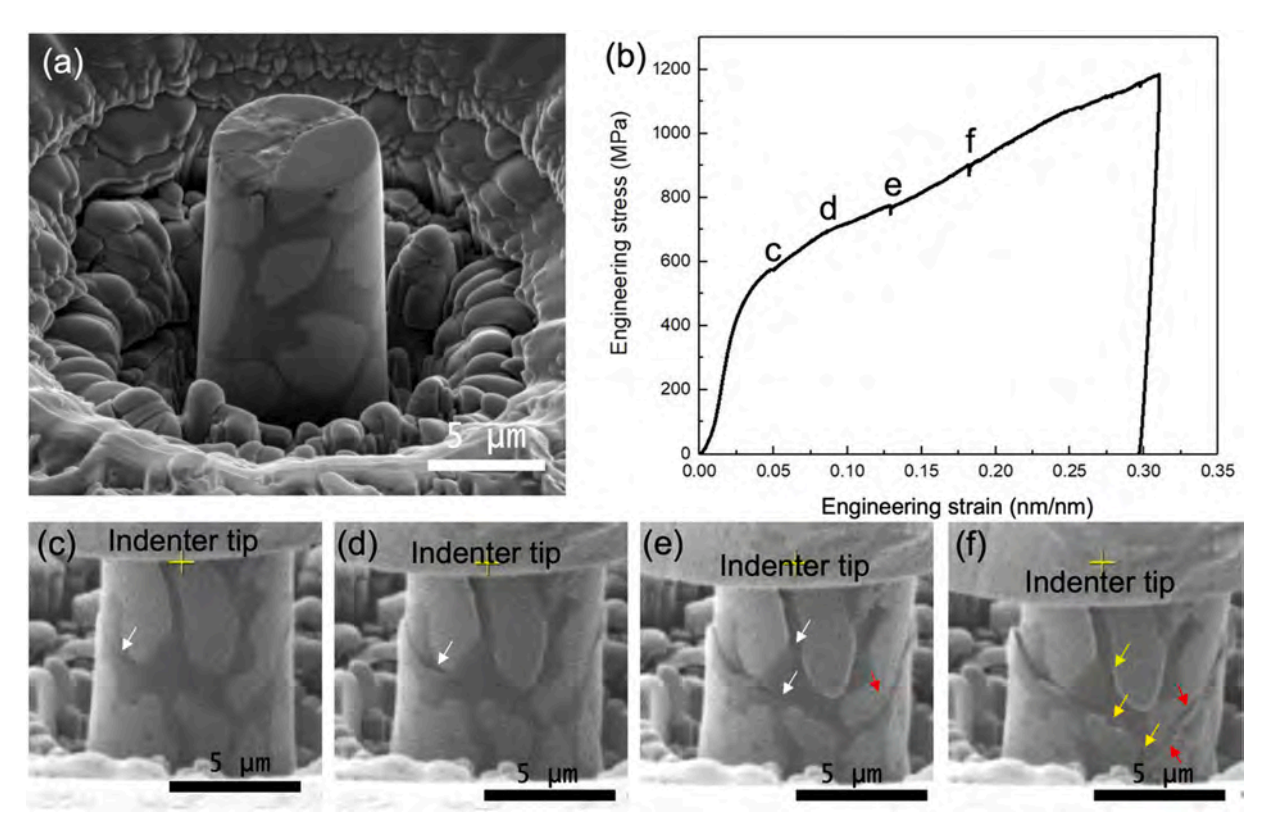


Fig. 2. (a) Representative SEM secondary electron micrograph of an Al-Al₃Ni micro-pillar before compression tests. (b) Engineering stress-strain curve for micro-pillar compression. (c-f) Screenshots from in-situ video at different compressive displacements, as shown in (b). Shear bands in Al are marked by the white arrows; shear bands and cracks are marked by the red arrows; and deformation induced interfacial cavities are marked by the yellow arrows.

in Fig. 2(b). The side-by-side in-situ SEM video and the corresponding load-displacement curve recorded during one of the compression tests are shown in Supplemental Information Video 1 (the movie play-speed is 5 times of the real-time). At the initial stage of plastic deformation, deformation strain is predominantly localized in the soft Al phase, as demonstrated by the formation and propagation of shear bands in the Al domain. The formation of shear band traces on the micro-pillar surface, as marked by the white arrow in Fig. 2(c), is concurrent with a small but noticeable stress drop on the stress-strain curve. Further propagation of the shear bands in the Al phase is effectively blocked by the hard Al₃Ni phase at the Al/Al₃Ni interfaces, as marked by the white arrow in Fig. 2 (d): this is considered to be one of the predominant strengthening mechanisms in this material. Shear band interaction with the hard Al₃Ni phase promotes the activation of additional shear bands in the Al phase at higher critical strength, as marked by the white arrows in Fig. 2(e), and therefore more homogeneous deformation of the micro-pillar. Interaction of dislocations in the Al phase with the Al/Al₃Ni interface will induce deformation and cracking of the Al₃Ni dendrites, as labeled by red arrows in Fig. 2(e and f). Finally, at higher strain, cavities are observed at the Al/Al₃Ni interfaces, as marked by yellow arrows in Fig. 2 (f). These interfacial cavities can potentially lead to debonding between the Al and Al₃Ni phases during further loading. Evolution of the strain field in the micro-pillars during in-situ deformation could be analyzed in the future by digital image correlation techniques [31] to better examine the localized deformation and failure mechanisms.

Supplementary material related to this article can be found online at doi:10.1016/j.addma.2022.103365.

Fig. 3(a) shows the calculated engineering stress-strain curves for two different micro-pillars prepared from two different cell wall regions. Interestingly, despite the well-known local variations in microstructure of AM processed materials, both samples behave reproducibly, which provides support to the reliability of the data. Please note that the stress drop before unloading for the \sim 17.5 % compressed sample is caused by

probe vibration when we manually interrupted the test (see Video 2 in the Supplemental Information). Key compressive properties for the cell walls are summarized in Table 1, in comparison with the bulk properties from the literature for Al 6061 [19] and the DED-deposited bulk hybrid Al-Al₃Ni metallic foam [18]. Though Al 6061 and the DED-deposited foam have yield strength values of only 55 MPa [19] and 190 MPa, respectively, the cell wall exhibits a yield strength of ~560 MPa and a Young's modulus of \sim 110 GPa (obtained from the unloading step). Notice that the density value is calculated based on a volume fraction of Al₃Ni of \sim 60 %. Given this, the Young's modulus of the Al-Al₃Ni is in good agreement with the Voigt upper bound value, indicating that the reinforcement topology is mechanically very efficient. The specific yield strength of the Al-Al₃Ni micro-pillar is approximately 162 kNm/kg, which is slightly higher than that for the DED-deposited hybrid Al-Al₃Ni metallic foam of 116 kNm/kg [18]. Due to the significant differences in both density and yield strength values, the calculated specific yield strength values ultimately are quite similar. Though compression tests are not suitable to evaluate ductility, it is important to note that the Al-Al₃Ni micro-pillars can withstand a large compressive strain of more than 30 % without a catastrophic stress drop.

Supplementary material related to this article can be found online at doi:10.1016/j.addma.2022.103365.

3.3. Post-mortem characterization of the deformation microstructure

SEM micrographs of the micro-pillars, deformed under compression up to engineering strains of ~ 17.5 % and 30 % are shown in Fig. 3(b) and (c), respectively. At a compressive strain level of 17.5 %, it is observed that, although most shear band traces in the Al phase are blocked by the Al₃Ni dendrites, some shear bands can transmit across the Al-Al₃Ni interface, causing slip band formation in the Al₃Ni phase, indicating that the Al₃Ni intermetallic is deformable to some extent at room temperature. Although Al₃Ni is normally brittle at low

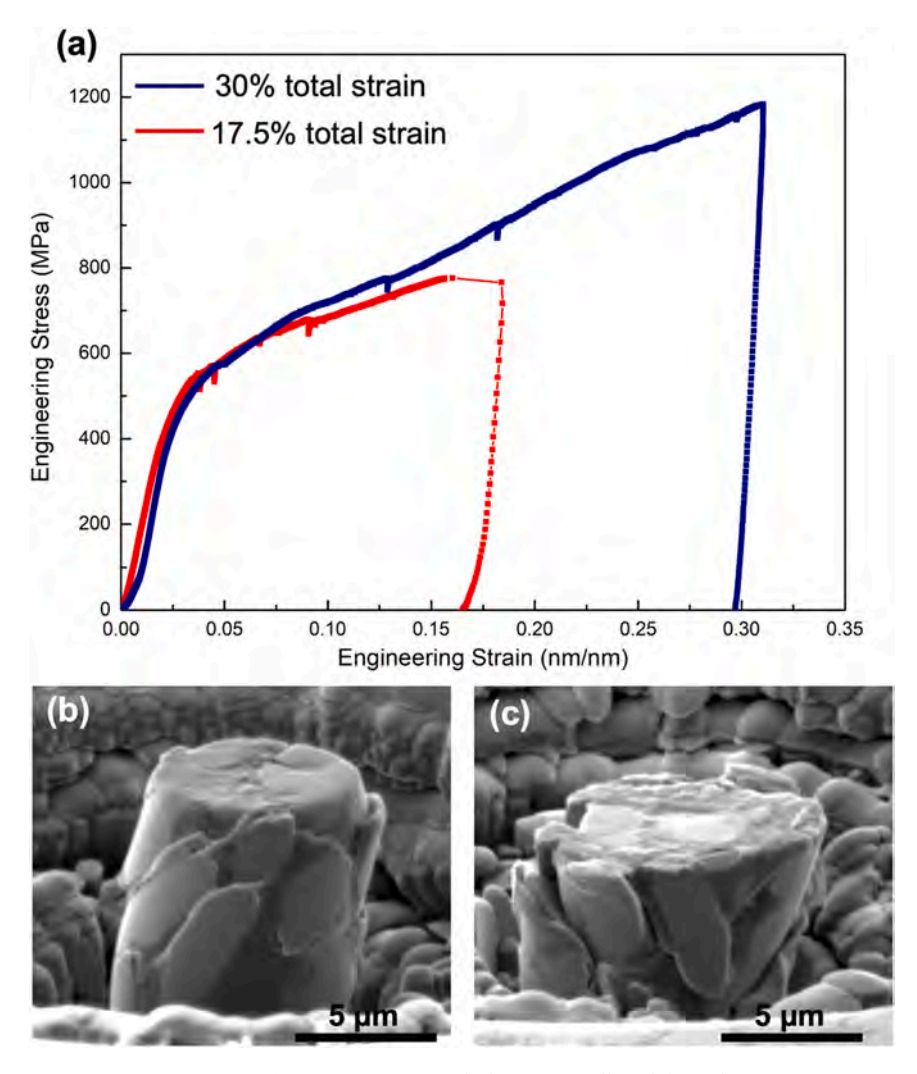


Fig. 3. (a) Compressive engineering stress-strain curves of two representative Al-Al₃Ni micro-pillars deformed to engineering strains of 17.5 % and 30 %. SEM secondary electron micrographs of the deformed micro-pillars to engineering strains of (b) 17.5 % and (c) 30 %, corresponding to the stress-strain curves in (a).

 $\label{table 1} \begin{tabular}{ll} \textbf{Compressive properties obtained from the cell wall in comparison with mechanical properties of Al 6061, Al_3Ni and the DED-deposited hybrid Al-Al_3Ni metallic foam. \end{tabular}$

Material	Al 6061 [19]	Al ₃ Ni [32]	Cell walls of Al- Al ₃ Ni metallic foam	Al-Al ₃ Ni metallic foam [18]
Density (g/cm ³)	2.7	4.0	3.5‡	1.6
Yield strength (MPa)	55*	-	560 ± 20	190
Specific yield strength (kN·m/ kg)	20*	-	162 ± 6	116
Young's modulus (GPa)	69	140	110 ± 10	8+

 $[\]ddagger$ Calculated density based on the area fractions of Al alloy and Al_3Ni phases measured from the SEM images.

temperatures, dislocations have been observed in Al_3Ni in a centrifugal cast $Al-Al_3Ni$ at room temperature after a special repeated loading-unloading tests [33]. The formation of cavities at the Al/Al_3Ni interface is also evident in Fig. 3(b). At an increased strain level of 30 %, multiple slip bands within the Al_3Ni phase can be observed. Furthermore, cracks formed along the Al/Al_3Ni interface, causing the Al_3Ni

phase to slide due to partial debonding between the ${\rm Al_3Ni}$ and the ${\rm Al}$ phase.

To investigate the microstructure in the plastically deformed region. PED characterization was performed on a TEM specimen lifted out from the 17.5 % compressed micro-pillar. Fig. 4(a) shows a low magnification bright field STEM image of the deformed micro-pillar. Inset are the TEM selected area electron diffraction (SAED) patterns for the FCC Al phase and orthorhombic Al₃Ni dendrites. The streak-like diffraction spots for the Al phase indicate that different subdomains within the selected grain exhibit slightly different crystal orientations. PED was performed on this specimen in the area marked by a red rectangle in Fig. 4(a). Fig. 4(b) shows the phase map, with red and green color representing the Al₃Ni and Al phases, respectively. The fraction of Al₃Ni measured from the PED phase map is ~ 60.7 %, which is consistent with that estimated by SEM on the surfaces of the micro-pillars. Boundaries with $> 5^{\circ}$ misorientations are superimposed onto the phase map, showing a high density of sub-grain boundaries is present in the Al phase, particularly near the Al/Al₃Ni interfaces, after in-situ compression. Fig. 4(c) is the corresponding orientation map for the two phases, color coded relative to the Z direction, with the inverse pole figure (IPF) color key shown below. The color variation in the Al phase illustrates that the misorientation and local strain are higher adjacent to the Al₃Ni dendrites, while much less deformation-induced misorientation is seen in the Al₃Ni phase. In addition, the orientation map also suggests an orientation relationship with 011Al||010Al₃Ni. Moreover, cracks and cavities are

⁺ Measured along the deposition direction.

O tempered Al 6061.

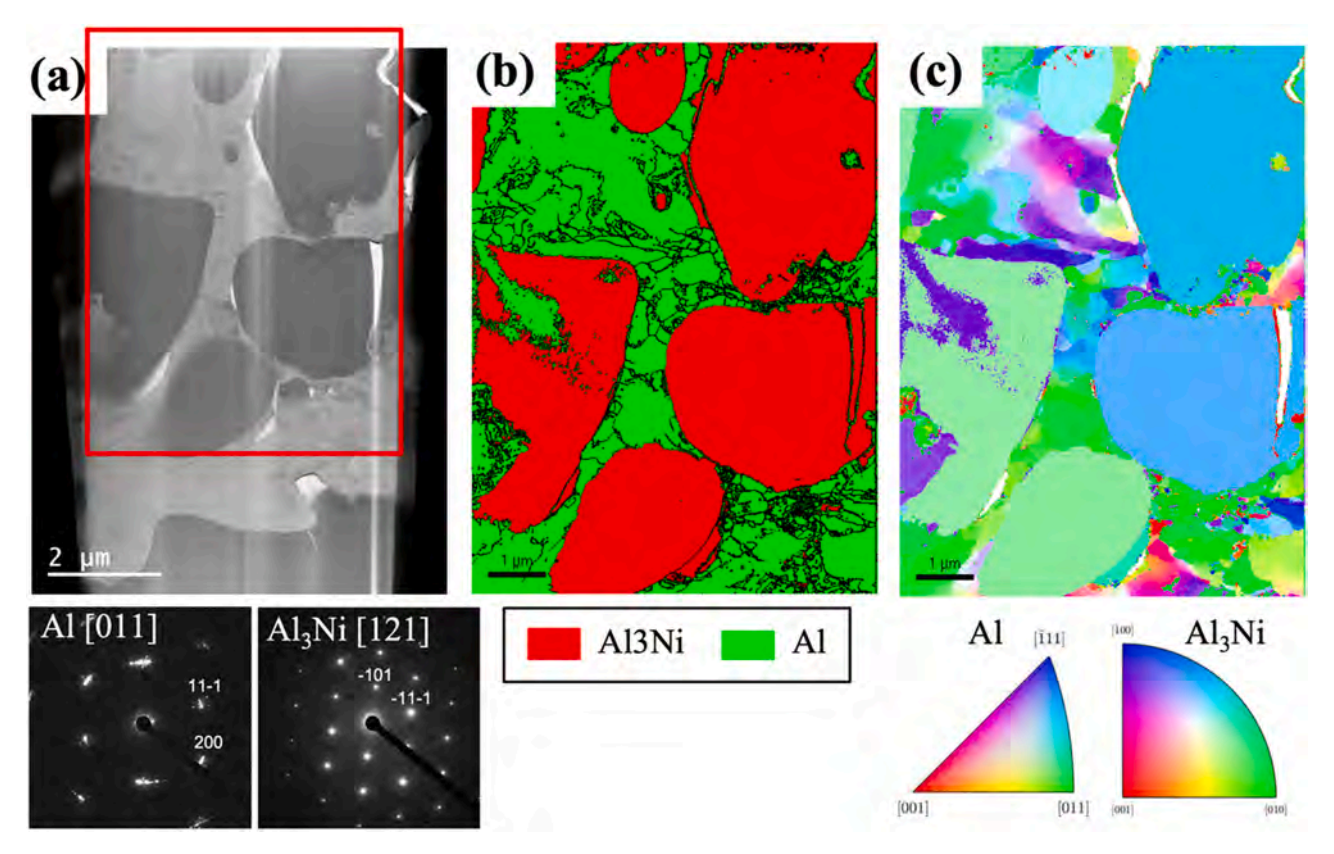


Fig. 4. Post-mortem precession electron diffraction (PED) characterization of the Al-Al₃Ni micro-pillar compressed to 17.5 % engineering strain: (a) Bright field STEM image of the micro-pillar. Inset are the selected area electron diffraction (SAED) patterns for the Al and Al₃Ni phases, respectively. (b) Boundaries with $> 5^{\circ}$ misorientation angles are superimposed onto the PED phase map. (c) Grain orientation map.

found within the Al₃Ni phases and at the Al/Al₃Ni interface.

To probe the deformation mechanisms of the cell walls at the nanoscale, detailed TEM characterization was also performed on the 17.5 % deformed micro-pillar. A high density of dislocations is observed in the Al phase, as seen in the bright field TEM image in Fig. 5(a). It is noted that the as-deposited metallic foam contains a dislocation density of $3.2 \times 10^{14} \, \text{m}^{-2}$ in the Al phase due to the nonequilibrium heating and cooling during DED processing and the large mismatch in thermal expansion coefficients of Al₃Ni and Al [18]. Therefore, we attribute the high dislocation density observed here in the Al phase to both the DED process and in-situ compression. Although dislocation impingement on the Al/Al₃Ni interfaces may induce stress concentrations, the majority of Al/Al₃Ni interfaces remain intact after deformation, as seen in Fig. 5(b). Sub-grain domains in the Al phase show different contrasts in the bright field images in Fig. 5(a and b), which is consistent with the high density of sub-grain boundaries in Fig. 4(b). Sub-grain boundaries are possibly formed by the self-assembly of the high density of dislocations in the Al phase.

Besides deformation of the relatively soft Al phase, our TEM analysis indicates room temperature plastic deformation of the relatively hard Al₃Ni dendrites. Fig. 5(c) shows slip bands in an Al₃Ni grain, which are likely initiated from the Al/Al₃Ni interface due to the high stress concentration and propagated into the grain interior. Although we are not able to provide direct evidence of slip transmission across the Al/Al₃Ni interface due to the high density of dislocations and severe local misorientations in the Al phase (as seen in Figs. 4(c) and 5(a-b)), slip transmission from Al to Al₃Ni has been previously reported in an Al-Al₃Ni composite prepared by centrifugal casting [33]. We hypothesize that the transmission of glide dislocations across the Al/Al₃Ni interface can transfer plastic deformation from the Al phase into the Al₃Ni phase and therefore alleviate stress concentration at the interfaces. The observations of slip bands in Al₃Ni nucleate from the Al/Al₃Ni interface,

and that the Al/Al₃Ni interface remains intact after deformation suggests the bonding strength of the interface is higher than the stress required for slip band nucleation in Al₃Ni, which is important for the co-deformation of Al and Al₃Ni in the cell walls. The strong Al/Al₃Ni interfaces in this material are therefore significant for the slip transfer between the Al and Al₃Ni phases and the observed plastic deformation of Al₃Ni. However, due to its mixed covalent and ionic bonding characteristics, the intermetallic Al₃Ni is not able to accommodate large stress/strain concentration at room temperature [34,35]. The limited deformability is visible in another Al₃Ni grain in Fig. 5(d), which contains multiple intersecting slip bands. Mutual intersection of slip bands in Al₃Ni causes high stress/strain concentration, which leads to the formation of nanocracks along the slip bands. Intragranular fracture of the Al₃Ni dendrites will finally lead to cracking and debonding along the Al-Al₃Ni interface upon further deformation.

To further understand the deformation behavior of the cell walls containing Al and Al₃Ni phases, MD simulations were performed. Fig. 6 (a) shows the initial atomic structure of the bi-crystal model. Dislocation evolution with increasing compressive strain is shown in Fig. 6(b). The green lines represent 1/6 <112> Shockley dislocations, and the purple lines represent 1/6 <110> stair-rod dislocations. Please note that due to the limitation of our visualization tool, dislocations in the orthorhombic structure Al₃Ni are not shown. Instead, the corresponding shear band evolution is shown in Fig. 6(c) to demonstrate the deformation history caused by the glide of dislocations. Initially, the bi-crystal system has a perfect structure without any defects. At strain of 11 %, dislocations nucleate in the Al phase to compensate the strain, whereas no plastic deformation is observed in the Al₃Ni phase. When strain was further increased to 18 %, the Al phase has multiple shear bands that are distributed homogeneously, and a shear band is formed in the Al₃Ni phase. At strain of 30 %, more shear bands are activated in both the Al and the Al₃Ni phases, with strain distribution in Al₃Ni being more

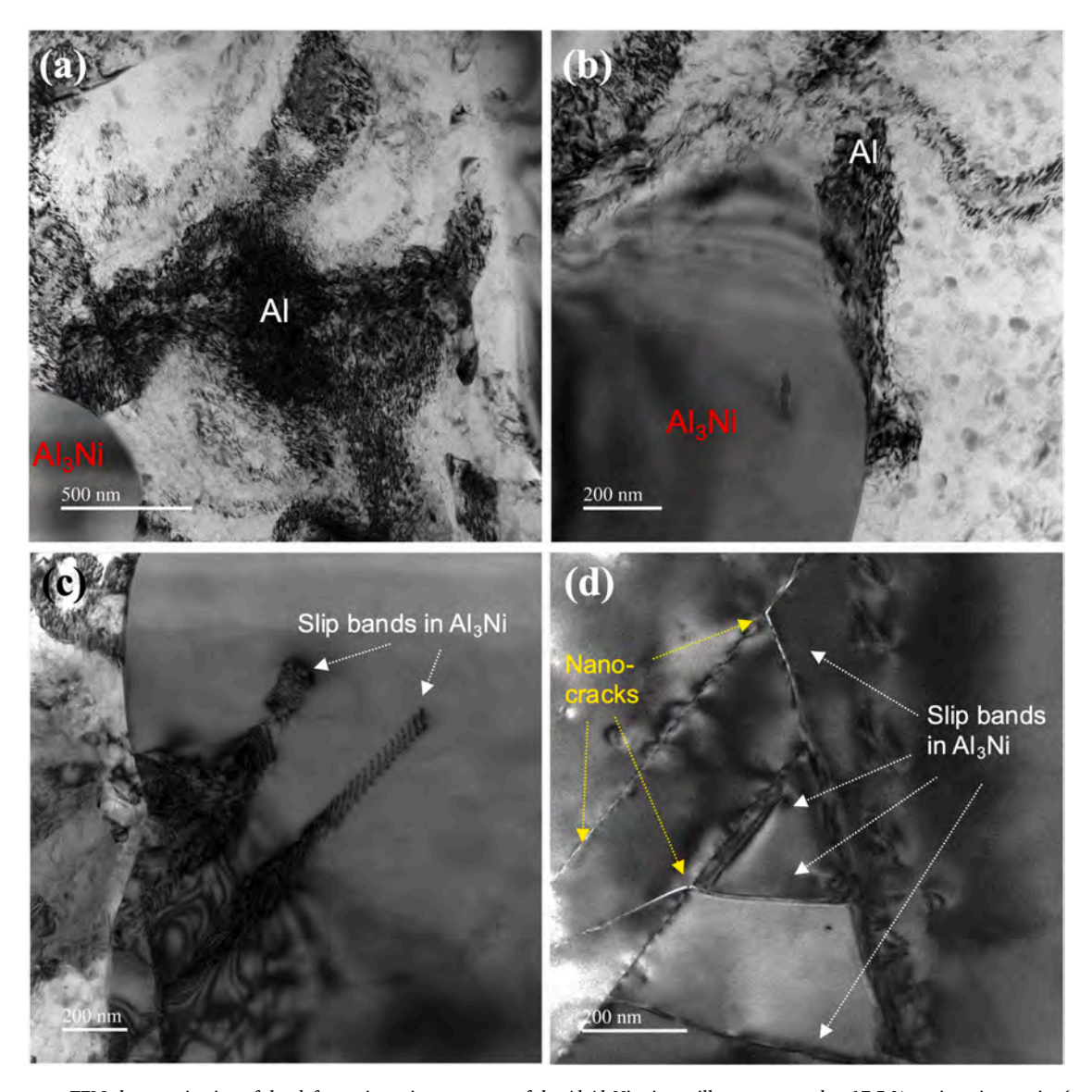


Fig. 5. Post-mortem TEM characterization of the deformation microstructure of the Al-Al $_3$ Ni micro-pillar compressed to 17.5 % engineering strain: (a and b) Bright field TEM images of the Al phase and near the Al/Al $_3$ Ni interface showing a high density of dislocations. (c) TEM of an Al $_3$ Ni dendrite grain with multiple slip bands nucleated from the Al/Al $_3$ Ni interface. (d) STEM image of a Al $_3$ Ni dendrite grain with intersecting slip bands, which leads to crack formation.

localized compared to that in the Al phase. Due to the differences in the simulated and experimental samples in size, microstructure of Al and Al $_3$ Ni phases and Al $_4$ Al $_3$ Ni interfaces, as well as strain rate, quantitative comparison of their mechanical property values and the critical strain levels is not feasible. Regardless, the MD simulations provide insights into the evolution of deformation mechanisms with an increase in deformation strain, as well as the important role of the Al $_4$ Al $_3$ Ni interface in obstructing dislocation motion.

Our MD simulation results indicate that dislocations are first nucleated in the Al phase, which is expected because Al is softer than the Al₃Ni phase. Due to the high crystallographic symmetry of the FCC system, nucleation of dislocations is homogeneous in Al. The phase boundary works as a barrier to impede the transmission of dislocations from the Al phase to the Al₃Ni phase, which leads to dislocation pile-up at the phase boundary. When the pile up stress reaches a critical value, the dislocations will pass the phase boundary and enter the Al₃Ni phase. The localized shear bands in the Al₃Ni phase are consistent with our experimental results (Fig. 5(c) and (d)), and are likely due to the lower symmetry of the orthorhombic structure of Al₃Ni. Although our current model was not designed to explore the interface strength, future modeling efforts that allow interfacial failure to be investigated would

be of interest.

4. Conclusions

An Al-based hybrid metallic foam was fabricated using DED additive manufacturing. The deformation behavior and the strengthening mechanisms of the cell wall regions within the foam were investigated via in-situ SEM micro-pillar compression, followed by post-mortem microstructural characterization using S/TEM and PED. The micropillars exhibit a yield strength of ~560 MPa and Young's modulus of \sim 110 GPa. The latter is in good agreement with the Voigt upper bound for a composite material, demonstrating that the dendritic reinforcement topology of Al₃Ni is mechanically very efficient. Deformation of the cell wall region occurs in the following sequence as the applied load is increased: a). shear bands formation and propagation in Al, b). shear bands impingement on the Al/Al₃Ni interfaces and the activation of additional slip systems in Al, c). localized slip band formation and intersection in the Al₃Ni phase, which causes cracking due to the associated stress concentration, and d). cracking and debonding of the Al/ Al₃Ni interfaces. Post-mortem microstructural analyses demonstrate a high density of dislocations and sub-grain boundaries in the Al alloy

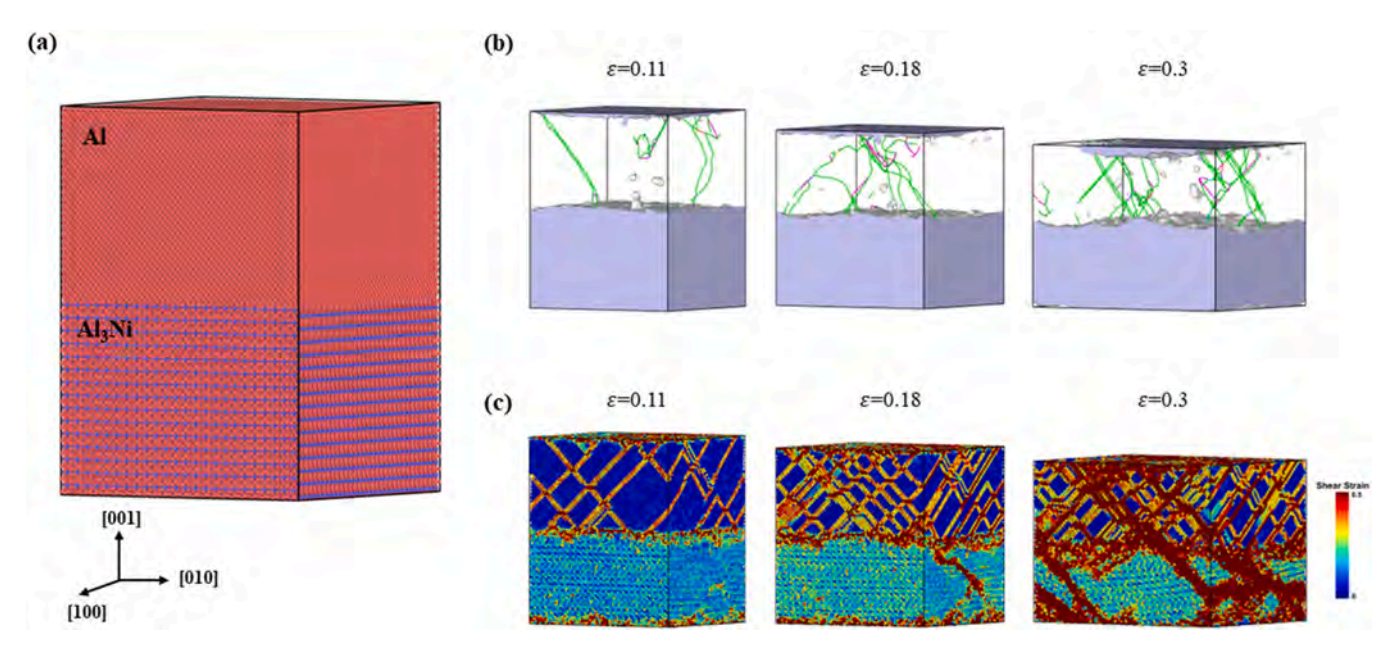


Fig. 6. MD simulation of Al-Al₃Ni under compressive deformation: (a) Structure of the Al-Al₃Ni bi-crystal model. (b) Dislocation evolution with compressive strain. Note only dislocations in the Al phase are shown. (c) Shear band evolution with compressive strain.

phase, particularly in the region adjacent to the Al/Al_3Ni interfaces, as well as localized slip bands formation in the Al_3Ni phase. MD simulation of an $Al-Al_3Ni$ bi-crystal shows, during compression, a uniform distribution of shear bands first form in Al and shear transfer from Al to Al_3Ni occurs when the pile up stress at the Al/Al_3Ni interface is sufficient. Our results unveiled the deformation mechanisms and suggested that the strong bonding strength of the Al/Al_3Ni interface, which allows signific stress transfer between the soft Al phase and the hard Al_3Ni phase, is critical for the superior elastic modulus and yield strength observed. Furthermore, the inherent brittleness of the Al_3Ni phase, which leads to crack initiation along the slip bands and slip band intersections, is likely limiting the room temperature mechanical properties of the cell wall of the Al-based metallic foam. High temperature mechanical properties of this material, when dislocation motion is easier in Al_3Ni , are therefore interesting for further investigations.

CRediT authorship contribution statement

Xin Wang: Conceptualization, Methodology, Investigation, Writing - Original Draft, Writing - Review & Editing. Baolong Zheng: Conceptualization, Methodology, Writing - Review & Editing. Hangman Chen: Methodology, Investigation, Writing - Original Draft, Writing - Review & Editing. Dongxu Liu: Investigation, Writing - Review & Editing. Kehang Yu: Investigation, Writing - Review & Editing. Benjamin E. MacDonald: Investigation, Writing - Review & Editing. Lorenzo Valdevit: Writing - Review & Editing. Lizhi Sun: Funding acquisition, Writing - Review & Editing, Penghui Cao: Conceptualization, Writing - Review & Editing, Funding acquisition. Enrique J. Lavernia: Conceptualization, Writing - Review & Editing, Funding acquisition. Julie M. Schoenung: Conceptualization, Writing - Review & Editing, Funding acquisition.

Declaration of Competing Interest

The authors declare that they have no known competing financial interests or personal relationships that could have appeared to influence the work reported in this paper.

Data Availability

Data will be made available on request.

Acknowledgments

The authors gratefully acknowledge support from the U.S. Army Research Office (W911NF2010264) and the National Science Foundation (DMR-2105328). We also acknowledge funding from the ONR–Defense University Research Instrumentation Program under grant N00014-11-1-0788, which supported the purchase of the Bruker/Hysitron Picoindentor system, and the use of facilities and instrumentation at the UC Irvine Materials Research Institute (IMRI), which is supported in part by the National Science Foundation through the UC Irvine Materials Research Science and Engineering Center (DMR-2011967). SEM work was performed using instrumentation funded in part by the National Science Foundation Center for Chemistry at the Space-Time Limit (CHE-0802913). Three dimensional CT images were conducted using instrumentation funded by the National Science Foundation (CMMI-1229405).

References

- C.G. Mahadev, K.M.Shivakumar Sreenivasa, A review on prodution of aluminium metal foams, IOP Conf. Ser.: Mater. Sci. Eng. 376 (2018), 012081, https://doi.org/ 10.1088/1757-899X/376/1/012081.
- [2] O. Tripathi, D.P. Singh, V.K. Dwivedi, M. Agarwal, A focused review on aluminum metallic foam: processing, properties, and applications, Mater. Today.: Proc. 47 (2021) 6622–6627, https://doi.org/10.1016/j.matpr.2021.05.099.
- [3] J. Marx, A. Rabiei, Overview of composite metal foams and their properties and performance, Adv. Eng. Mater. 19 (2017) 1600776, https://doi.org/10.1002/ adem.201600776.
- [4] P. Sevilla, C. Aparicio, J.A. Planell, F.J. Gil, Comparison of the mechanical properties between tantalum and nickel–titanium foams implant materials for bone ingrowth applications, J. Alloy. Compd. 439 (2007) 67–73, https://doi.org/ 10.1016/j.jall.com.2006.08.069.
- [5] J. Banhart, Manufacture, characterisation and application of cellular metals and metal foams, Prog. Mater. Sci. 46 (2001) 559–632, https://doi.org/10.1016/ S0079-6425(00)00002-5.
- [6] K. Yang, X. Yang, E. Liu, C. Shi, L. Ma, C. He, Q. Li, J. Li, N. Zhao, Elevated temperature compressive properties and energy absorption response of in-situ grown CNT-reinforced Al composite foams, Mater. Sci. Eng.: A 690 (2017) 294–302, https://doi.org/10.1016/j.msea.2017.03.004.
- [7] C.M. Cady, G.T. Gray, C. Liu, M.L. Lovato, T. Mukai, Compressive properties of a closed-cell aluminum foam as a function of strain rate and temperature, Mater. Sci. Eng.: A 525 (2009) 1–6, https://doi.org/10.1016/j.msea.2009.07.007.
- [8] J. Zhang, L. Chen, H. Wu, Q. Fang, Y. Zhang, Experimental and mesoscopic investigation of double-layer aluminum foam under impact loading, Compos. Struct. 241 (2020), 110859, https://doi.org/10.1016/j.compstruct.2019.04.031.

- [9] T. Fiedler, K. Al-Sahlani, P.A. Linul, E. Linul, Mechanical properties of A356 and ZA27 metallic syntactic foams at cryogenic temperature, J. Alloy. Compd. 813 (2020), 152181, https://doi.org/10.1016/j.jallcom.2019.152181.
- [10] E. Linul, O. Khezrzadeh, Axial crashworthiness performance of foam-based composite structures under extreme temperature conditions, Compos. Struct. 271 (2021), 114156, https://doi.org/10.1016/j.compstruct.2021.114156.
- [11] S. Yu, Y. Luo, J. Liu, Effects of strain rate and SiC particle on the compressive property of SiCp/AlSi9Mg composite foams, Mater. Sci. Eng.: A 487 (2008) 394–399, https://doi.org/10.1016/j.msea.2007.11.025.
- [12] E. Linul, D. Pietras, T. Sadowski, L. Marşavina, D.K. Rajak, J. Kovacik, Crashworthiness performance of lightweight composite metallic foams at high temperatures, Compos. Part A: Appl. Sci. Manuf. 149 (2021), 106516, https://doi. org/10.1016/j.compositesa.2021.106516.
- [13] C. Wang, C. Guo, R. Qin, F. Jiang, Fabrication and characterization of layered structure reinforced composite metal foam, J. Alloy. Compd. 895 (2022), 162658, https://doi.org/10.1016/j.jallcom.2021.162658.
- [14] B. Katona, G. Szebényi, I.N. Orbulov, Fatigue properties of ceramic hollow sphere filled aluminium matrix syntactic foams, Mater. Sci. Eng.: A 679 (2017) 350–357, https://doi.org/10.1016/j.msea.2016.10.061.
- [15] M. Taherishargh, E. Linul, S. Broxtermann, T. Fiedler, The mechanical properties of expanded perlite-aluminium syntactic foam at elevated temperatures, J. Alloy. Compd. 737 (2018) 590–596, https://doi.org/10.1016/j.jallcom.2017.12.083.
- [16] B. Katona, A. Szlancsik, T. Tábi, I.N. Orbulov, Compressive characteristics and low frequency damping of aluminium matrix syntactic foams, Mater. Sci. Eng.: A 739 (2019) 140–148, https://doi.org/10.1016/j.msea.2018.10.014.
- [17] I.N. Orbulov, A. Szlancsik, A. Kemény, D. Kincses, Compressive mechanical properties of low-cost, aluminium matrix syntactic foams, Compos. Part A: Appl. Sci. Manuf. 135 (2020), 105923, https://doi.org/10.1016/j. compositesa 2020 105923
- [18] B. Zheng, Y. Li, J.E. Smugeresky, Y. Zhou, D. Baker, E.J. Lavernia, Hybrid Al + Al₃Ni metallic foams synthesized in situ via laser engineered net shaping, Philos. Mag. 91 (2011) 3473–3497, https://doi.org/10.1080/14786435.2011.586375.
- [19] A.H. Committee, Properties and selection, Nonferrous Alloy. Spec. -Purp. Mater. (1990), https://doi.org/10.31399/asm.hb.v02.9781627081627.
- [20] J.T. Kim, V. Soprunyuk, N. Chawake, Y.H. Zheng, F. Spieckermann, S.H. Hong, K. B. Kim, J. Eckert, Outstanding strengthening behavior and dynamic mechanical properties of in-situ Al–Al₃Ni composites by Cu addition, Compos. Part B: Eng. 189 (2020), 107891, https://doi.org/10.1016/j.compositesb.2020.107891.
- [21] C. Suwanpreecha, P. Pandee, U. Patakham, C. Limmaneevichitr, New generation of eutectic Al-Ni casting alloys for elevated temperature services, Mater. Sci. Eng.: A 709 (2018) 46–54, https://doi.org/10.1016/j.msea.2017.10.034.
- [22] R. Kakitani, R.V. Reyes, A. Garcia, J.E. Spinelli, N. Cheung, Relationship between spacing of eutectic colonies and tensile properties of transient directionally

- solidified Al-Ni eutectic alloy, J. Alloy. Compd. 733 (2018) 59–68, https://doi.org/ 10.1016/j.iallcom.2017.10.288.
- [23] T.P.D. Rajan, R.M. Pillai, B.C. Pai, Functionally graded Al–Al3Ni in situ intermetallic composites: Fabrication and microstructural characterization, L4–L7, J. Alloy. Compd. 453 (2008), https://doi.org/10.1016/j.jallcom.2006.11.181.
- [24] H. Okada, Y. Fukui, R. Sako, N. Kumazawa, Numerical analysis on near net shape forming of Al-Al₃Ni functionally graded material, Compos. Part A: Appl. Sci. Manuf. 34 (2003) 371–382, https://doi.org/10.1016/S1359-835X(03)00023-X.
- [25] H. Zhang, B.E. Schuster, Q. Wei, K.T. Ramesh, The design of accurate microcompression experiments, Scr. Mater. 54 (2006) 181–186, https://doi.org/ 10.1016/j.scriptamat.2005.06.043.
- [26] M.D. Uchic, P.A. Shade, D.M. Dimiduk, Plasticity of micrometer-scale single crystals in compression, Annu. Rev. Mater. Res. 39 (2009) 361–386, https://doi. org/10.1146/annurev-matsci-082908-145422.
- [27] Y. Mishin, Atomistic modeling of the γ and γ'-phases of the Ni–Al system, Acta Mater. 52 (2004) 1451–1467, https://doi.org/10.1016/j.actamat.2003.11.026.
- [28] A.P. Thompson, H.M. Aktulga, R. Berger, D.S. Bolintineanu, W.M. Brown, P. S. Crozier, P.J. in 't Veld, A. Kohlmeyer, S.G. Moore, T.D. Nguyen, R. Shan, M. J. Stevens, J. Tranchida, C. Trott, S.J. Plimpton, LAMMPS a flexible simulation tool for particle-based materials modeling at the atomic, meso, and continuum scales, Comput. Phys. Commun. 271 (2022), 108171, https://doi.org/10.1016/j.cpc.2021.108171.
- [29] A. Stukowski, Visualization and analysis of atomistic simulation data with OVITO-the open visualization tool, Model. Simul. Mater. Sci. Eng. 18 (2009), 015012, https://doi.org/10.1088/0965-0393/18/1/015012.
- [30] S.U. Nisa, S. Pandey, P. Pandey, A review of the compressive properties of closed-cell aluminum metal foams, 09544089221112291, Proc. Inst. Mech. Eng., Part E. J. Process Mech. Eng. (2022), https://doi.org/10.1177/09544089221112291.
- [31] Christoph Eberl (2022). Digital Image Correlation and Tracking (https://www.mathworks.com/matlabcentral/fileexchange/12413-digital-image-correlation-and-tracking), MATLAB Central File Exchange.
- [32] Y. Fukui, K. Takashima, C.B. Ponton, Measurement of Young's modulus and internal friction of an in situ Al-Al₃Ni functionally gradient material, J. Mater. Sci. 29 (1994) 2281–2288, https://doi.org/10.1007/BF00363415.
- [33] K. Yamashita, I. Fujimoto, T. Murakumo, S. Kumal, A. Sato, Observation of glide dislocations in D020 ordered Al₃Ni, Philos. Mag. A 80 (2000) 219–235, https:// doi.org/10.1080/01418610008212050.
- [34] B. Cantor, G.J. May, G.A. Chadwick, The tensile fracture behaviour of the aligned Al-Al₃Ni and Al-CuAl₂ eutectics at various temperatures, J. Mater. Sci. 8 (1973) 830–838, https://doi.org/10.1007/BF02397911.
- [35] Y. Fukui, N. Yamanaka, Y. Enokida, Bending strength of an Al-Al₃Ni functionally graded material, Compos. Part B: Eng. 28 (1997) 37–43, https://doi.org/10.1016/ S1359-8368(96)00018-2.